Post-Print of an Accepted Manuscript on the Laboratory of Turbulent Flows Website

Complete citation:

Wang, S., & Ghaemi, S. (2019). Three-dimensional wake of nonconventional vortex generators. *AIAA Journal*, *57*(3), 949-961. doi: 10.2514/1.J057420

The final publication is available at https://doi.org/10.2514/1.J057420

The Accepted Manuscript begins on the next page.

Three-dimensional Wake of Non-Conventional Vortex Generators

Sen Wang[1] and Sina Ghaemi[2]

Department of Mechanical Engineering, University of Alberta, Edmonton, Alberta, T6G 1H9, Canada

The wake flows of wishbone, doublet, and ramp type vortex generators (VGs) were investigated. The VGs were placed in the thin laminar boundary layer of a flat plate at a Reynolds number of 930 based on the free-stream velocity and height (*h*) of the VGs. The turbulence statistics in the wake of the VGs were measured with high spatial-resolution using planar particle image velocimetry (PIV) and stereoscopic PIV (stereo-PIV). Three-dimensional time-resolved tomographic PIV (tomo-PIV) was also carried out to visualize the evolution of vortices. A fastest recovery of the wake deficit was observed for the wishbone VG. The peak of turbulence production in the wake of the wishbone and doublet VGs had a similar magnitude and was 1.5 times stronger than that of the ramp VG. The hairpin vortices generated by the ramp VG formed the largest percentage of the wake turbulent kinetic energy and their size is about half that of the hairpins produced by the wishbone and doublet VGs. The wishbone and the ramp VGs had the best overall performance. The wishbone VG generated the strongest mixing in the wake region while the ramp VG had the smallest drag coefficient. The doublet VG had the weakest overall performance, as it was not efficient in mixing the flow and had the largest parasitic drag.

I.Nomenclature

c	=	vortex generator chord length (mm)
e	=	wake recovery number
h	=	vortex generator height (mm)
f	=	focal length of camera lens
u	=	streamwise fluctuating velocity (m/s)
v	=	wall-normal fluctuating velocity (m/s)
x	=	streamwise direction
y	=	wall-normal direction
z	=	spanwise direction

[1] MSc student, Department of Mechanical Engineering, University of Alberta, sen6@ualberta.ca
[2] Assistant Professor, Department of Mechanical Engineering, University of Alberta, ghaemi@ualberta.ca

P = turbulence production (m^2/s^3)
Q = Q-criterion vorticity tensor ($1/s^2$)
U = instantaneous streamwise velocity (m/s)
U_∞ = free-stream velocity (m/s)
V = instantaneous wall-normal velocity (m/s)
W = instantaneous spanwise velocity (m/s)
β = incidence angle between the side-edge of VG and free-stream (degree)
δ = boundary layer thickness (mm)
Ω_x = streamwise vorticity (1/s)

II.Introduction

Boundary layer separation from a surface can occur due to an adverse pressure gradient (APG) or a sharp geometric discontinuity. This process has been described as an initial rapid thickening of the boundary layer followed by the lift-up of the flow from the surface by a large wall-normal velocity [1]. The blockage of the free-stream by the separated flow and the roll-up of the shear layer reduce the efficiency of pressure recovery systems such as diffusers [2]. Flow separation also increases drag, reduces lift, and causes strong structural vibration on lifting surfaces such as wings and high-lift devices. In most aerodynamic systems, peak performance is limited by flow separation. Therefore, the development of passive and active techniques for separation control has been sought. Applying vortex generators (VGs) has proven to be a successful passive approach.

VGs are surface-mounted protrusion, and are widely applied as passive flow control devices to delay or prevent flow separation. In the wake of a VG, vortices transfer the high momentum flow from the free-stream to the near-wall region [3]. This effectively reduces the thickness of the boundary layer, relaxes the adverse pressure gradients, and provides the fluid with sufficient streamwise momentum to remain attached to the wall [3]. As a result, flow separation is prevented or postponed to a downstream location.

An early investigation of VGs was carried out by Taylor [4] by installing a row of small wall-mounted vanes at an angle with respect to the free-stream to created streamwise vortices. The height (h) of these vane-type VGs was on the order of the boundary layer thickness (δ). Schubauer and Spangenberg [3] investigated the geometrical effect of large VGs ($h \sim \delta$) with various shapes on the development of a turbulent boundary layer under an adverse pressure gradient. They observed that all VGs reduced the adverse pressure gradient by transferring high velocity flow to the near-wall region. The early VGs could prevent flow separation and increase lift; however, due to their relatively large size, they also increased the parasitic drag.

The drag penalty of VGs can be reduced by deploying the VGs only when flow separation is anticipated. For example, it is desirable to deploy VGs during landing or take-off of a flight when large lift is needed and to retract the VGs during the cruise phase to reduce drag. However, active deployment of the VGs can increase the

complexity of the system. Another approach to reduce the parasitic drag is to use low-profile VGs with $h/\delta \sim 0.1$ to 0.5. The height is carefully selected to effectively inhibit flow separation with minimal drag penalty. In 1972, Kuethe [5] introduced a wavy surface with semi-circular elements inclined 15º with respect to the flow direction. The elements were submerged in the boundary layer ($h/\delta \sim 0.27$-0.42) and it was conjectured that they enhanced mixing by generating quasi-streamwise vortices. The low-profile VGs applied by Kuethe [5] were successful in reducing acoustic noise by suppressing the Kármán vortex street. The measurement of the flow field conducted on a high-lift airfoil shows that the streamwise vortices produced by the low-profile VGs are almost completely dissipated downstream of the separation region [6]. Therefore, the Kuethe's wavy surface is an effective method for flow control that is not accompanied by an unnecessary drag penalty [6]. Vortex generators based on a wedge-element profile is another variation that were first introduced by Wheeler [7, 8]; these are referred to as non-conventional VGs in this study. They were designed to produce stronger vortices than the vane-type VGs in order to provide sufficient flow mixing with a lower device height. The most common non-conventional VGs are known as the doublet [7], wishbone [8], and ramp as seen in Fig.1. These VGs are mechanically stronger and easier to implement than the vane-type VGs [9].

Several investigations have evaluated the dependency of geometrical parameters such as incidence angle (the angle between the vane body and the flow direction), chord length, and device height on the performance of VGs. The experiment of Godard and Stanislas [10] on vane-type VGs showed that the optimum incidence angle between the side-edge of the VG and the free-stream is about 18°. Experimental investigations by Lin [6] and the numerical study of Forster and White [11] demonstrated that a longer chord is required to generate stronger vortices. The height of the low-profile VGs are typically scaled as $h/\delta \sim 0.2$ so that the local velocity at this height is over 75% of the free-stream velocity [6]. Further increase of the height only moderately improves separation control while significantly increasing drag [6]. Lin et al. [6, 12, 13] performed a series of experiments on a backward-facing ramp, and observed that the doublet and reverse wishbone VGs have the best performance when $h/\delta \sim 0.1$ and $h/\delta \sim 0.2$, respectively. The result from Lin et al. [12, 13, 14] and Lin [6] proved that the low-profile VGs, such as the reverse wishbone VG and the vane-type VG, with $h/\delta \sim 0.2$, are as effective as the traditional large VGs with $h/\delta \sim 0.8$ in delaying the separation [15].

The effectiveness of a VG also depends on its installation location. A low-profile VG performs best when placed 5-30h upstream of a fixed separation line [6]. Based on oil visualizations conducted by Lin [12], the optimum

location to install the doublet and wishbone VGs falls between 3-10h upstream of the separation baseline. A numerical study of ramp type VGs on a cambered wing by Forster and White [11] demonstrated that VGs are more effective when placed at the point of maximum velocity.

In terms of phenomenological understanding and visualization of the flow physics, the oil-flow visualization of Schubauer and Spangenberg [3] demonstrated that VGs that produce streamwise vortices are more effective in transporting momentum towards the wall than VGs that generate transverse vortices [6]. Lin et al. [12, 13] showed that larger transport of momentum to the near-wall region can be accomplished by non-conventional VGs with wedge element and vane-type VGs with a V-shape arrangement that produce pairs of counter-rotating streamwise vortices. The effectiveness of vane-type VGs with a V-shape configuration has also been confirmed by Betterton et al. [16] and Janiszewska et al. [17]. Lin [6] demonstrated that wall-normal triangular or trapezoidal vanes arranged in a V-shape configuration effectively generate counter-rotating vortices. Rao and Kariya [18] investigated the effectiveness of low-profile VGs (height = 0.6δ) with vane-type and semi-circular geometries. They measured static pressure and loss of total pressure to evaluate the VGs for control of APG-induced separation over a flat plate. Their results showed that pairs of vane-type VGs in a V-shaped arrangement are less sensitive to the geometric parameters of the elements, such as height, incidence angle, and chord length. However, there have been a limited number of investigations on the effect of the shape of non-conventional VGs on the wake flow.

Previous studies revealed that the dominant vortical structure in the wake of vane-type VGs in a V-shape arrangement is a pair of counter-rotating streamwise vortices. For instance, early smoke visualization showed that, in the wake of wedge-element VGs, a pair of streamwise counter-rotating vortices is generated [19]. The same flow pattern has also been observed in the wake of various VGs in V-shape configurations through Laser Doppler Anemometry (LDA) [6, 16], two-dimensional PIV [10], velocity probe measurements [20], and numerical simulations [11]. An early investigation on the hairpin vortex generated by a hemispherical element in a laminar boundary layer was provided by Acarlar and Smith [21] to demonstrate the evolution process of hairpin vortices. The hairpin vortex contains a transverse vortex head, an inclined neck due to the shear layer profile, and a pair of streamwise vortex legs [21]. The ejection and sweep events formed by the hairpin head and streamwise legs transfer the momentum. As the legs move together downstream, they undergo a mutual cancellation due to the viscous interaction between two opposite vortex cores, which reduces their core vorticity and the corresponding ejection event. The tip is unaffected by this mechanism while it continues to diffuse. Due to measurement limitations in the

past several decades, the major focus has been on characterization of two-dimensional mean flow profiles; three-dimensional characterization of the coherent structures has been rarely investigated. With the development of tomo-PIV, the three-dimensional instantaneous wake region can be measured quantitatively. For example, the tomo-PIV measurements conducted by Sun et al. [22] and Ye et al. [23] captured the hairpin vortex and its evolution within the instantaneous wake of micro-ramp VGs in a supersonic turbulent boundary layer and an incompressible transitional wake, respectively. The investigations [22, 23, 24] highlight the importance of characterizing the coherent structures towards understanding the mechanism of mixing and separation control by different VGs.

Here we investigate the near-wake region of three non-conventional VGs with wishbone, doublet, and ramp shapes installed in a thin laminar boundary layer. The objective is to characterize the turbulence statistics and the three-dimensional coherent structures in the wake flow. Planar-PIV and stereo-PIV are applied to characterize the velocity, Reynolds stresses, and vorticity fields with high spatial-resolution in one *x*-*y* and two *y*-*z* planes across the wake region. The spatial organization of the generated vortical structures and the temporal evolution of the vortical structures are investigated using tomo-PIV. The main aim is to identify the mixing mechanism and the effect of each VG shape on the flow development.

III.Description of Experiment

The flow facility and the geometry of the VGs are described in this section. Planar-PIV and stereo-PIV are applied for measurement with high-spatial resolution in a limited number of wake cross-sections. Time-resolved tomo-PIV is applied for volumetric visualization of the wake and to study the evolution of vortical structures.

A. Flow facilities

The measurements were conducted in a closed-loop water flume. The test section is 10 m long and has a rectangular cross-section 50 cm high (water level) and 75 cm wide. A flat plate with a half-wedge leading edge at zero angle-of-attack was installed vertically. The flow speed U was set to 0.155 m/s to form a thin laminar boundary layer. The VGs were installed at l = 65 mm downstream of the plate leading edge at $\mathrm{Re}_l \approx 10{,}100$, defined as $\rho Ul/\mu$ where ρ and μ are density and kinematic viscosity of water, respectively. The corresponding laminar boundary layer thickness (δ) is calculated based on the Blasius solution [25] following

$$\frac{\delta}{l} = \frac{4.91}{\sqrt{Re_l}}. \quad (1)$$

The estimated boundary layer thickness is 3.2 mm at a location 65 mm downstream of the flat plate leading-edge. The natural transition location is determined to be 3.2 m from the leading-edge according to the critical Re_l = 500,000. Hence the flat plate will be entirely covered by laminar flow when VGs are absent. The shape factor has also been estimated based on the planar-PIV measurement of the velocity profile and is 2.8 at this location. The low *Re* and shape factor indicate a laminar boundary layer immediately upstream of the VG. This allows wake formation without any interaction with vortices coming from an upstream turbulent boundary layer.

B. Vortex generators

Three VGs with wishbone, doublet, and ramp type geometries were investigated as shown in Fig. 1. The VGs were 3D-printed using Form 2 printer (Formlabs) with clear resin to prevent strong reflection of the laser light. After 3D printing, the VGs were carefully polished using a polishing compound (Tamiya) without affecting the overall geometry. The printing material has less than 1% weight gain when immersed in water for 24 hours. The immersion time of the VGs was kept short (~few hours) to prevent any possible water absorption and deformation. The geometric dimensions include the height (h), chord length (c), incidence angle (β), and frontal area, and were kept constant for all VGs. This prevents any scaling effect and allows for investigating the effect of VG shape on the downstream wake. The geometric dimensions of the VGs are summarized in Table 1. The VG wetted area indicates the surface area of the VG which is contact with the flow. The total wetted area includes the surface area of the VG and the wetted surface surrounding the VG. In order to highlight the geometrical effect of the VG shape, the added area is minimized by only covering the wall from the leading edge of the VG to the trailing edge in the streamwise direction and 6h in the spanwise direction. The spanwise dimension is selected to be consistent with the drag evaluation performed in VG performance section. This area is considered to also include the effect of boundary layer drag in the calculated drag from the momentum deficit method. The dimensions of the VGs results in a height-based Reynolds number (Re_h) of 930, which makes the study applicable to unmanned aerial vehicles (UAVs) with a cruising speed of up to 10 m/s in air. The coordinate system is shown in Fig. 1a with its origin at the trailing edge of the VG. The x-, y-, and z-axis indicate streamwise, wall-normal, and spanwise directions, respectively.

Table 1 The geometric dimensions of the wishbone, doublet, and ramp VG.

VG	Height (h), mm	Chord length (c), mm	Incidence angle (β), degree	Frontal area, mm^2	VG wetted area (mm^2)	Total wetted area (mm^2)
Wishbone	6.0	36.0	25.0	108	560	1989
Doublet	6.0	36.0	25.0	108	1060	1993
Ramp	6.0	36.0	25.0	108	850	1875

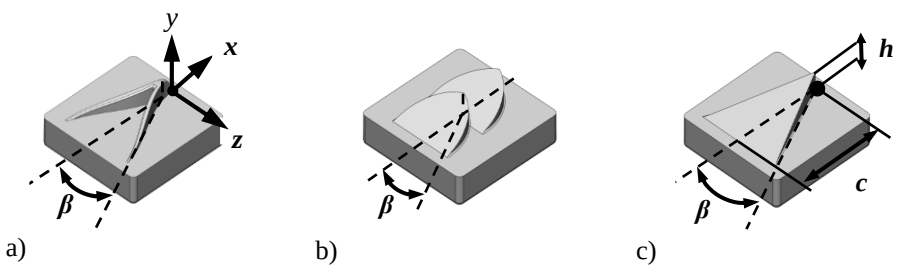

Fig. 1 The 3D models of the (a) wishbone, (b) doublet, and (c) ramp VGs.

C. Planar particle image velocimetry

A planar-PIV experiment was carried out to measure the 2D flow statistics in an *x*-*y* plane along the centerline of the VGs, as shown in Fig. 2. The experiment consisted of an Imager Intense (LaVision GmbH) 12-bit CCD camera with a sensor size of 1040×1376 pix and pixel size of 6.45 × 6.45 μm^2. The camera was equipped with a Nikon lens with a focal length of f = 105 mm at aperture setting of f / 5.6 to image a 44.1×58.3 mm^2 field-of-view (FOV). The digital resolution of the imaging system was 42.4 μm/pix and the depth-of-focus was 3.8 mm. The FOV is specified as FOV1 in Fig. 2 and is equivalent to 7.35h × 9.72h in terms of the VG height h. It covers 9.16h in the streamwise direction (x) downstream from the VG trailing edge, and 7.35h in the wall-normal direction from the wall surface. A laser sheet of approximately 1-mm thickness was generated using an Nd:YAG laser (Gemini, NewWave Research) with 110 mJ per pulse at 30 Hz. The flow was seeded using silver-coated 2 μm spherical glass beads (SG02S40 Potters Industries) with a density of 4 g/cm^3. A set of 1,500 double-frame images was collected for each VG using a pulse separation of Δt = 3300 μs at 5 Hz. Image pre-processing was conducted to improve the signal-to-noise ratio (SNR) by subtracting the minimum intensity of each ensemble from each image. The images were also normalized using the ensemble averages. The vector fields were obtained using a double-frame cross-correlation with a multi-pass algorithm and a final interrogation window (IW) size of 32 × 32 pixel (1.36 × 1.36 mm^2) at 75% overlap in Davis 8.3 (LaVision GmbH). The universal outlier detection method was applied to remove spurious vectors [25].

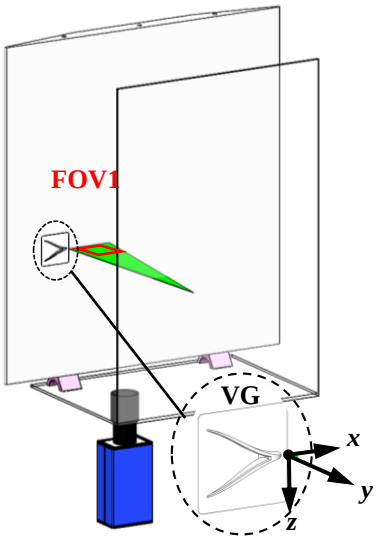

Fig. 2 A schematic of the planar-PIV measurement.

D. Stereoscopic particle image velocimetry

Stereoscopic particle image velocimetry (stereo-PIV) was carried out to characterize the streamwise vorticity with high spatial ~~-~~resolution in two *y*-*z* planes across the wake as shown in Fig. 3. The stereo-PIV setup consisted of two Imager Intense (LaVision GmbH) CCD cameras with a solid angle of about 100º with respect to each other~~,~~ as shown in Fig. 3. Scheimpflug adapters were equipped to correct the focus planes. The two fields-of-view~~s~~ at the upstream and downstream locations are indicated as FOV2 and FOV3 within the figure with dimensions of 35 × 41 mm^2 (5.83*h* × 6.83*h*) and a digital resolution of 29.4μm/pix. The cameras were equipped with Nikon lenses with *f* = 105 mm and aperture settings of *f* / 11, which provided a depth-of-focus of approximately 8 mm. A laser sheet with 2 mm thickness was formed to accommodate the large out-of-plane motion of the particles while capturing their smaller in-plane motion in the *y* and *z* directions. The same Nd:YAG laser (Gemini, NewWave Research) and tracer particles as the planar-PIV experiment were used. The initial calibration of the imaging system was performed using a two-dimensional glass sheet with a grid of black circles. The target was imaged at three *x* locations by moving it ± 0.5 mm with respect to the center of the laser sheet (*y*-*z* plane at *x* = 0). The mapping of the calibration image was carried out using a third-order polynomial fit in Davis 7.4 (LaVision GmbH). A set of 1,500 images was collected for each VG at a frame rate of 5 Hz and a laser pulse separation of Δ*t* = 1000 μs. The self-calibration procedure was carried out following Wieneke [26] in Davis 8.3 (LaVision GmbH) with a root-mean-square (RMS) fit of 0.74 pixels. The SNR of the images was improved by subtracting the minimum intensity of each ensemble from each image and normalizing the images using the ensemble average in Davis 8.3. Vector fields were obtained using the stereoscopic cross-correlation method with a multi-pass algorithm and a final IW size of 32 × 32 pixel (0.94 × 0.94 mm^2) at 75% overlap. Images were post-processed using universal outlier detection to remove spurious vectors [26].

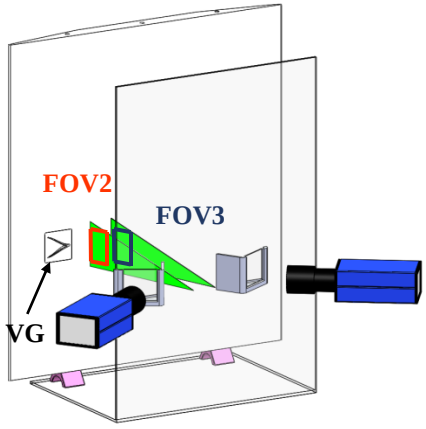

Fig. 3 A schematic of the stereo-PIV measurement.

E. Tomographic particle image velocimetry

The three-dimensional organization of vortices in the wake of the VGs and their temporal evolution was characterized using tomo-PIV. The tomo-PIV system consisted of four v611 Phantom cameras imaging the illuminated volume in the arrangement shown in Fig. 4. Each camera has a sensor size of 1280 × 800 pix with a pixel size of 20 × 20 μm^2. The cameras were equipped with Scheimpflug adapters and Nikon lenses with focal lengths of f =105 mm. The apertures were set to f / 16 for all cameras with an estimated depth-of-field of 14 mm. The viewing angle between the left and right cameras was 60° while the viewing angle between the top and bottom cameras was about 40°. Due to the large viewing angle between left and right cameras, two glass prisms were installed to improve the image quality~~,~~ as shown in Fig. 4b. An Nd:YLF (Dual-head DM20-527DH, Photonics Industries) with 20 mJ per pulse at 1 kHz was used to form a collimated laser sheet. The sheet was 13 mm thick in the y direction and 90 mm wide in x direction. To obtain a top hat intensity profile, the low intensity boundaries of the laser sheet were cropped using knife edges. To prevent the strong laser reflection from the flat plate, the laser sheet was offset by 2 mm from the surface of the flat plate. The illuminated volume covered 2 mm to 15 mm (2.5h) from the wall surface. The flow was seeded using hollow glass spheres (20 μm) that have a density about 1.10 g/cm^3 (110P8, Potters Industries).

The illuminated volume was 95×55×13 mm^3 (15h × 9h × 2.5h), which is equivalent to 1421 × 848 × 200 voxels in the x, z, and y direction, respectively. This corresponds to a digital resolution of 64.9 μm/pix (magnification of 0.3). The useful section of the measurement volume started from the trailing-edge of the VGs at x = 0h and covered up to x = 10h. The seeding density was approximately 0.02 particles per pixel (ppp). The particle size was visually inspected to be around 2-4 pixels (diameter). The initial calibration of the four cameras was carried out using a 3D calibration target (type 11, LaVision GmbH) by fitting a third-order polynomial function. The initial disparity map showed a large image distortion with a 1-3 pixel~~s~~ residual. After applying the self-calibration, the residual RMS was reduced to 0.03 pixels, which is lower than Wieneke's [27] suggestion of 0.1 pixels.

A total of 3,500 time-resolved images were collected for each VG at a recording rate of 800 Hz. The frame rate allowed small particle displacement of 2-3 pixels between frames in order to apply a multi-frame correlation technique. To improve the SNR, the minimum intensity of each ensemble was subtracted from each image, and the images were normalized using an ensemble average. Further improvement was applied to the images by subtracting a local minimum and normalizing the intensity using a local average with a kernel of 100 pixels. The measurement

volume was reconstructed using the MART algorithm (Elsinga et al. [28]) in Davis 8.4 (LaVision, GmbH). A multi-frame cross-correlation was applied to calculate the vector fields using the volume deformation iterative multi-grid technique (VODIM) developed by Scarano and Poelma [29]. The vector information was obtained through the sliding-average of the correlation maps of three pairs of consecutive frames with Δt = 3.75 ms (equivalent to 267 Hz) to increase the SNR. The final window size was 32 × 32 × 32 voxels (2.08 × 2.08 × 2.08 mm^3) with 75% overlap.

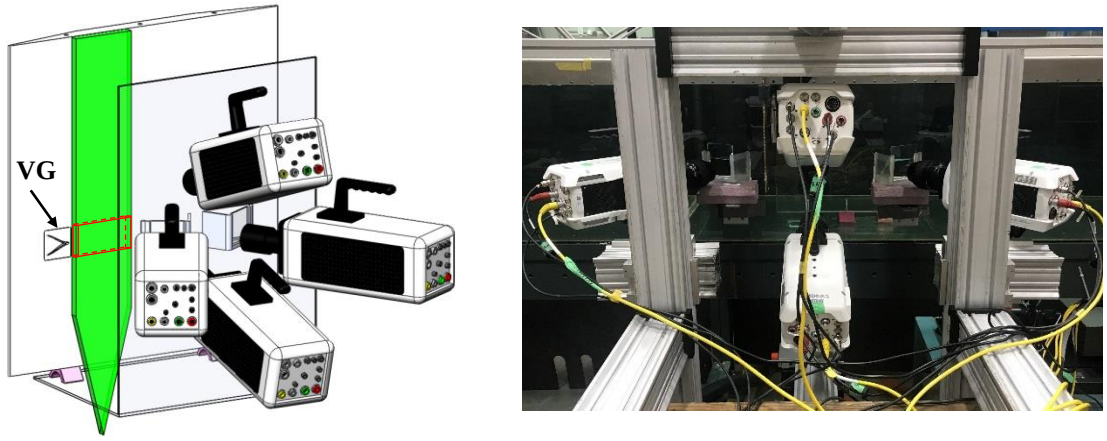

a) b)

Fig. 4 a) A schematic of the tomo-PIV measurement, and b) a photo of the experiment showing the camera configuration.

IV.Results

This section characterizes the wake flow of the three VGs by investigation of the mean flow, Reynolds stresses, turbulence production, vorticity field, and the dominant coherent structures. The instantaneous streamwise, wall normal, and spanwise velocities are indicated by U, V, and W. The average quantities are specified by < > while the fluctuating terms are indicated by lower case letters. The instantaneous velocity is decomposed as $U = \langle U \rangle + u$ following Pope's [30] notation.

A. Velocity deficit of the wake

The three-dimensional mean velocity from the tomo-PIV measurements in the immediate wake of the three VGs is shown in Fig. 5. The free-stream velocity, U_∞, is used to normalize the values of $\langle U \rangle$ and $\langle V \rangle$. The trailing edge of the VG is located at x = 0. The mean streamwise velocity component is presented using an iso-surface of $0.9U_\infty$ (yellow, light gray) to visualize the boundaries of the wake region. The wall-normal velocity components $\langle V \rangle/U_\infty$ are also shown using two iso-surfaces of positive and negative $0.05U_\infty$, indicated by green (medium gray) and blue (dark gray), respectively. The thresholds are selected to visualize the shape of the wake and the wall-normal

transport of fluid. The iso-surfaces of streamwise velocity show that the doublet VG has the widest wake in the spanwise direction. The top-side of the iso-surfaces in the *y*-direction are cropped at $y = 2.5h$, due to the limited measurement. However, it is still evident that the wakes of the wishbone and the doublet VG are farther extended than that of the ramp VG in the wall-normal direction. Overall, the comparison of the $0.9U_\infty$ iso-surfaces suggests that the doublet VG has the largest pressure drag due to the larger region with velocity deficit. All three VGs generate a consistent upward flow along the centerline of the wake as shown by the green (medium gray) iso-surfaces. The wishbone VG generates the largest region of upward motion while the ramp VG has the smallest region of upward motion. The downward velocity forms two streamwise regions elongated on both sides of the FOV, as shown by the blue iso-surfaces (dark gray). The downward velocity at $0.05U_\infty$ persists over a longer distance in the wake of the wishbone VG.

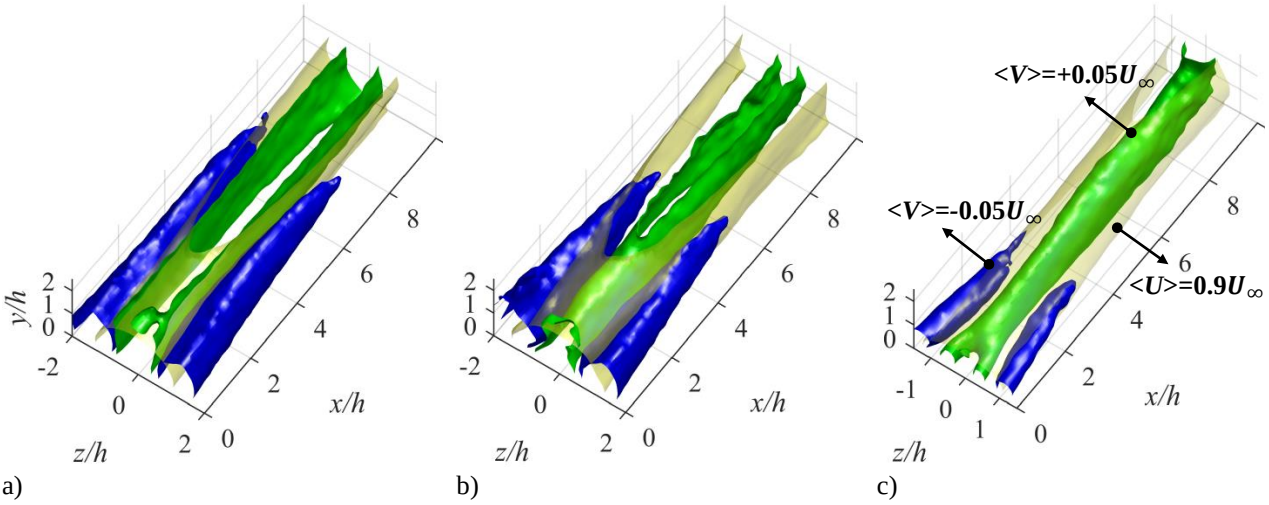

a) b) c)

Fig. 5 Mean velocity isosurfaces in the wake of the a) wishbone, b) doublet, and c) ramp VGs.

The distribution of mean streamwise velocity normalized using U_∞ from planar-PIV in the *x*-*y* plane and from stereo-PIV in the two *y*-*z* planes, is shown in Fig. 6. Since the flow is symmetric along the *x*-*y* plane at $z = 0$, the *y*-*z* planes from stereo-PIV is only shown for $z \geq 0$. The planar-PIV data and stereo-PIV data approximately match in the interface of the measurement planes. The observation from the *x*-*y* planes showed that the wishbone VG has the fastest velocity recovery. The velocity from the *x*-*y* plane of the wishbone wake recovers to $0.4\text{-}0.6U_\infty$ at $y \approx 0.6h$ after $x \approx 1h$. While in the wake of doublet and ramp VGs, recovery to $0.4\text{-}0.6U_\infty$ cannot be clearly observed in the FOV. The *y*-z planes show the existence of a local minimum streamwise velocity at approximately $z = 0.5h$. The *y*-*z* contours also reveal that the local minimum in the wake of the wishbone and doublet VGs is lifted as the flow

moves downstream and is at a higher y/h location in the y-z plane of x/h = 5. The contours show that the doublet and ramp VGs decelerate the flow more than the wishbone VG.

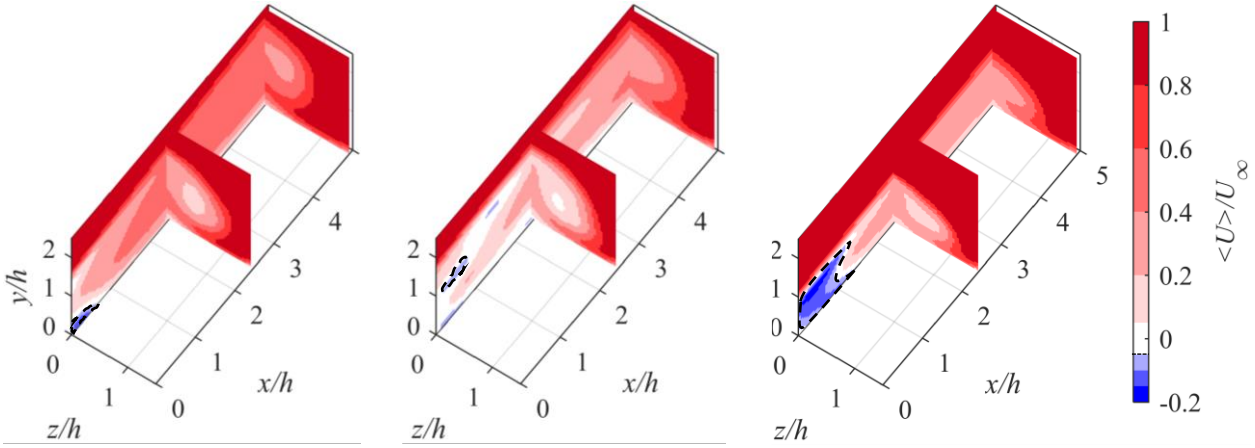

a) b) c)

Fig. 6 Mean normalized streamwise velocity $\langle U\rangle/U_\infty$ in the wake of the a) wishbone, b) doublet, and c) ramp VG.

To estimate the height of wake, the normalized mean streamwise velocity profile for each VG is plotted in Fig. 8 at three streamwise locations along the wake center. The height of the wake is characterized by the wall-normal position of the wake center, which is determined by the upper (labeled as point A) and lower inflection points (labeled as point B) of the $\langle U\rangle/U_\infty$ profiles [22]. Following the work of Ye et al. [22], the height of the wake h_{wake} is defined by the average height of point A and point B as

$$h_{\text{wake}} = \frac{y_{\text{up}} + y_{\text{low}}}{2}. \quad (1)$$

The variation in the height of the wake using this estimation is listed in Table 2. The wake of the wishbone VG expands by about 5% from $x = 4h$ to $x = 6h$, while its height remains approximately the same size before $x = 4h$. The wake height of the doublet and the ramp VGs fluctuate around $1.1h$ and $0.7h$, respectively.

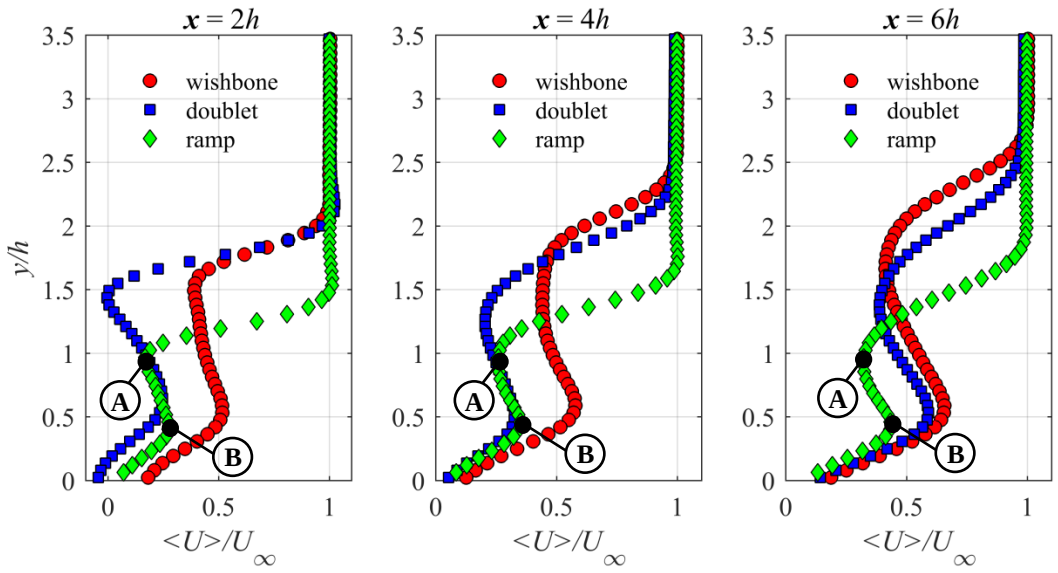

Fig. 7 Normalized streamwise velocity profiles at $x = 2h$, $x = 4h$ and $x = 6h$.

Table 2 Height of wake for each VG at different streamwise location.

VG	h_{wake} ($x = 2h$)	h_{wake} ($x = 4h$)	h_{wake} ($x = 6h$)
Wishbone	1.08h	1.08h	1.14h
Doublet	1.19h	1.08h	1.11h
Ramp	0.69h	0.72h	0.69h

The one-dimensional profiles of the velocity deficit (U_{def}) in the wake of the three VGs versus the streamwise distance are shown in Fig. 8 to evaluate wake recovery. The local minimum of streamwise velocity $\langle U \rangle_{min}$ is the velocity at the lower inflection point A [23], obtained from planar-PIV measurements in the x-y plane. The estimated $\langle U \rangle_{min}$ is used to calculate the velocity deficit as $U_{def} = 1 - \langle U \rangle_{min}/U_\infty$ and plotted versus x in Fig. 8 [22]. The flow recirculates and has a backward direction in the immediate downstream location of the doublet and ~~the~~ ramp VGs. Therefore, $U_{def} > 1$ at $x = 0$-$1.8h$ for the doublet and ~~the~~ ramp VGs. The velocity deficit recovers quickly to 40% of the free-stream velocity at $x \sim 2h$ behind the wishbone VG. The rate of recovery significantly decreases at $x = 2h$ and the velocity deficit stays around $0.57U_\infty$ until $x = 5.4h$. The wishbone and ramp VGs generate a smoother recovery trend compared to the doublet VG. There is a secondary peak in the velocity deficit of the doublet VG at $x = 4h$, which is associated with the interaction of the vortices shed from the second half-body of the double VG. The latter is inferred since the main difference between the doublet and other two VGs is the second-half body of the VGs. A power law fit cannot precisely characterize the velocity recovery effect at this near wake region of $x < 8h$. However, it could describe the recovery trend well in the investigations of Sun et al. [22] and Ye et al. [23] at farther downstream locations of $x = 7$-$27h$ behind the ramp VGs.

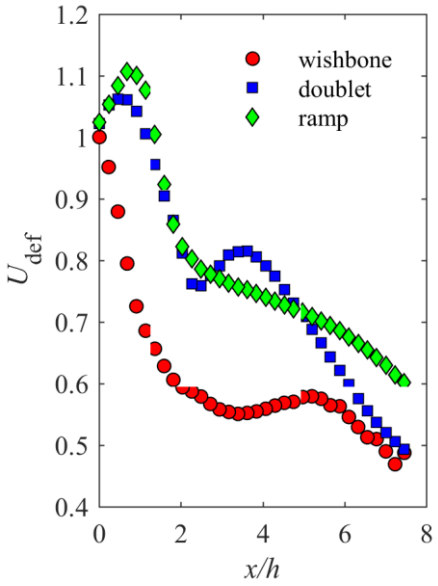

Fig. 8 Normalized velocity deficit in the wake of VGs.

B. Mean wall-normal and spanwise velocity

The mean wall-normal velocity contours for all the VGs are normalized using U_∞ and are presented in Fig. 9. For better visualization of the weaker downward velocity, a scaling factor of ~~×~~2× is applied to all ~~the~~ *y*-*z* planes. As seen in the *x*-*y* planes in Fig. 9, the wishbone VG has the strongest upward motion in the *y*-*z* plane, which confirms the observation based on tomo-PIV in Fig. 5. The most significant upward flow transport for the wishbone VG happens within $x = 1 - 4h$ with a velocity peak of $0.5U_\infty$. This strong wall-normal behaviour persists over a longer streamwise distance compared to the two other VGs. The doublet VG has the second strongest upward flow motion. However, the magnitude of the positive peak of $\langle V \rangle$ is approximately 63% of the peak of the wishbone VG at $x = 2.5h$. The ramp VG shows the weakest upward flow motion. The positive $\langle V \rangle$ has a magnitude between 0.1 and $0.2U_\infty$. The positive peak velocity is around 40% of the peak of the wishbone VG. The *y*-*z* planes from Fig. 9 show that the wishbone VG also has the strongest downward flow motion. The strongest downward motion appears at $z = 1h$ for all cases, and it is locally weaker compared to the upward motion. In general, the wall-normal fluid transport becomes weaker as the flow travels downstream.

The contours in Fig. 10 show the mean spanwise velocity $\langle W \rangle$ from stereo-PIV in the two *y*-*z* planes. The pattern of the spanwise motion is consistent with the direction of streamwise vortices inferred from the wall-normal velocity contours. The wishbone VG has the strongest spanwise motion, followed by the doublet VG. The ramp VG

produces the weakest spanwise motion. The dominant spanwise motion is the rotating motion toward the centerline of the wake at the near-wall region, and outward from the centerline at distances farther away from the wall. The wishbone VG presents a strong inward velocity of $0.2U_\infty$ at $x = 2.5h$, which remains strong at $x = 5h$. The doublet VG shows a similarly strong inward velocity pattern. The ramp VG is much weaker than the other two VGs. The upper outward motion is generally weaker compared to the inward motion, and decays downstream.

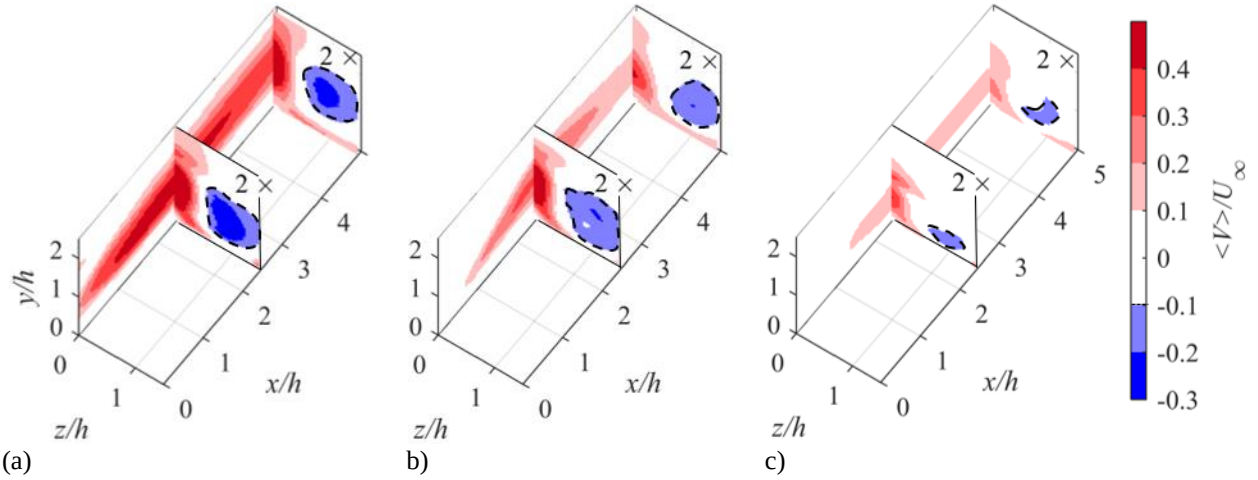

(a) b) c)

Fig. 9 Mean normalized wall-normal velocity $\langle V \rangle / U_\infty$ for the a) wishbone, b) doublet, and c) ramp VG.

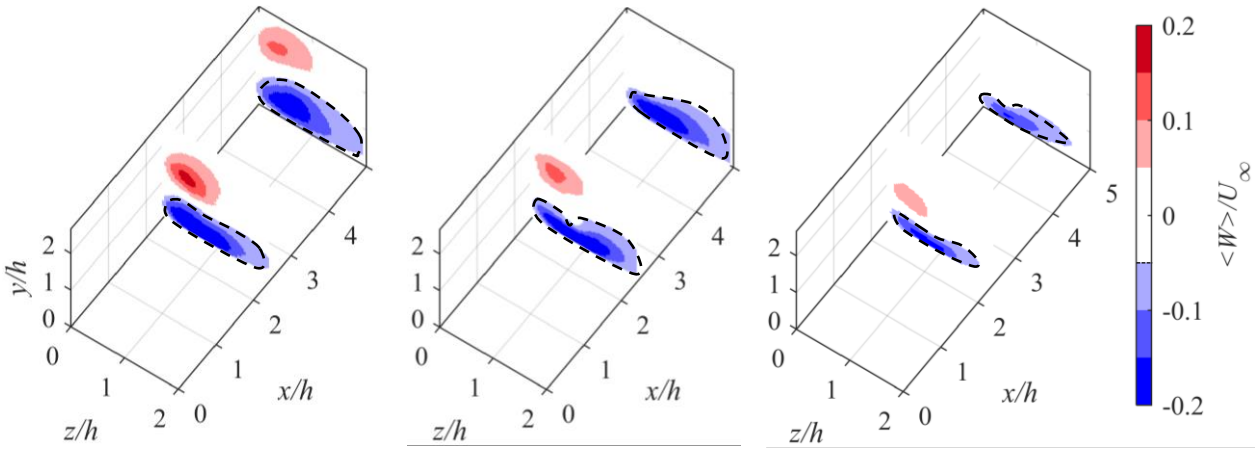

a) b) c)

Fig. 10 Mean normalized spanwise velocity $\langle W \rangle / U_\infty$ for the a) wishbone, b) doublet, and c) ramp VG.

Measurement of the mean velocity in the wake of the three VGs demonstrated that a pair of steady streamwise counter-rotating vortices are generated. This pair of vortices has also been observed in the previous studies. Betterton et al.'s [16] LDA measurement showed the same pattern in the wake of a ramp VG. Forster and White [11] conducted a numerical simulation using a shear stress transport model and showed a similar pattern behind a ramp-like VG. The vortex cores appear to be at $(y, z) = (1h, \pm 0.5h)$ in the $x = 2.5h$ plane, and at $(y, z) = (1.5h, \pm 0.5h)$ in

the $x = 5h$ plane behind the wishbone and ~~the~~ doublet VGs. In the wake of the ramp VG, the vortex cores are closer to each other and closer to the wall. The center of the vortex is at $(y, z) = (0.5h, \pm 0.2h)$ of $x = 2.5h$ and at $(y, z) = (1h, \pm 0.2h)$ of $x = 5h$ in the wake of the ramp VG. The observation also shows no obvious widening of the distance between the pair of vortices in the z direction~~,~~ within the range $x = 0$ to $5h$. However, the vortex cores lift up due to the self-induced velocity, which explains the increase in the height of the wakes in the contours of streamwise velocity. The stronger upward motion relative to the downward velocity is caused by the strong ejection event induced by the mutual effect of two counter-rotating streamwise vortices~~,~~ as described by Acarlar and Smith [21]. Based on the size of the wake region, the doublet VG is expected to cause the largest parasitic drag. The wishbone VG is more efficient in enhancing flow mixing due to stronger streamwise vortices and fastest recovery of the wake deficit.

C. Reynolds stress

The normal Reynolds stresses in the wake of the VGs are investigated here to characterize the strength of the turbulence fluctuations. The Reynolds stresses are an indication of unsteadiness in the wake and of small-scale mixing. The contours of the streamwise Reynolds stress, $\langle u^2 \rangle$, normalized by U_∞^2 from planar and stereo-PIV are shown in Fig. 11. As shown in the x-y planes, the peak of $\langle u^2 \rangle / U_\infty^2$ appears at the shear layer between the upper wake and the free-stream for all of the VGs. The high intensity layer of $\langle u^2 \rangle / U_\infty^2$ for the wishbone and doublet VGs thickens rapidly after $x \approx 2.5h$, while the ramp VG has a consistent thin layer of high intensity $\langle u^2 \rangle / U_\infty^2$ along the whole x-axis range. The thickening of the high intensity region is associated with the spanwise section of the hairpin vortices (i.e. the hairpin head). The hairpin heads generate strong ejection and sweep motions in the shear layer region. The magnitude of $\langle u^2 \rangle / U_\infty^2$ increases from the y-z plane at $x = 2.5h$ to the y-z plane at $x = 5h$ for all of the VGs. The doublet VG has the strongest $\langle u^2 \rangle / U_\infty^2$, followed by the wishbone VG. The ramp VG has a low $\langle u^2 \rangle / U_\infty^2$ in the y-z plane at $x = 2.5h$ and no contour is visible.

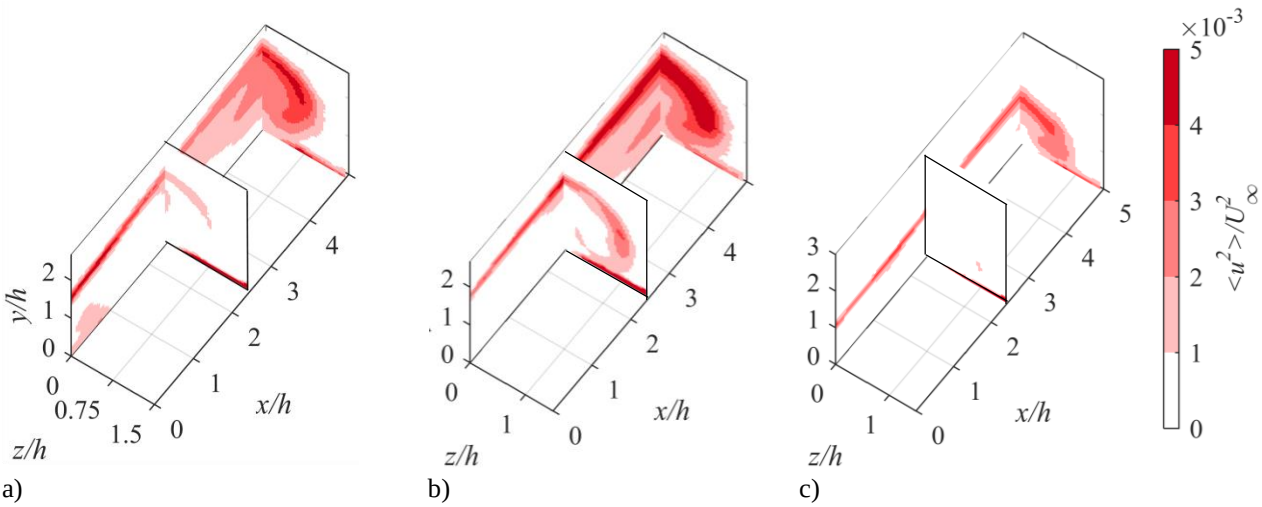

Fig. 11 Normalized streamwise Reynolds stress $\langle u^2\rangle/U_\infty^2$ for the a) wishbone, b) doublet, and c) ramp VGs.

The wall-normal Reynolds stress $\langle v^2\rangle$, normalized by U_∞^2, is presented in Fig. 12. The $\langle v^2\rangle$ is relatively weak in the near-wake region as observed in the *x*-*y* plane from planar-PIV. In the wake of the wishbone and doublet VGs, a significant $\langle v^2\rangle/U_\infty^2$ does not appear until $x = 2h$. For the ramp VG, $\langle v^2\rangle/U_\infty^2$ in the *x*-*y* plane is not visible until farther downstream at $x = 4h$. The high-intensity $\langle v^2\rangle/U_\infty^2$ layer for all of the VGs grows thicker and becomes stronger with an increase in streamwise distance. To better visualize the distribution of $\langle v^2\rangle/U_\infty^2$ across the *y*-*z* plane, a scaling factor of 3× is applied to the *y*-*z* planes for all three VGs. As observed in the *y*-*z* plane at $x = 2.5h$ in the wake of wishbone VG, the high intensity $\langle v^2\rangle/U_\infty^2$ tends to be concentrated in the shear layer between the wake and the free-stream. At the same cross-section in the wake of the doublet VG, the large $\langle v^2\rangle/U_\infty^2$ appears at the shear layer above the wake and at a spot near the wall. At $x = 2.5h$, no significant $\langle v^2\rangle/U_\infty^2$ can be observed in the wake of the ramp VG. The pattern of $\langle v^2\rangle/U_\infty^2$ in the *y*-*z* planes at $x = 5h$ is visualized without applying a scaling factor for all of the VGs. Similar to the result observed in Fig. 11, the doublet VG presents the most intense $\langle v^2\rangle/U_\infty^2$ and the ramp VG shows the smallest $\langle v^2\rangle/U_\infty^2$ contour.

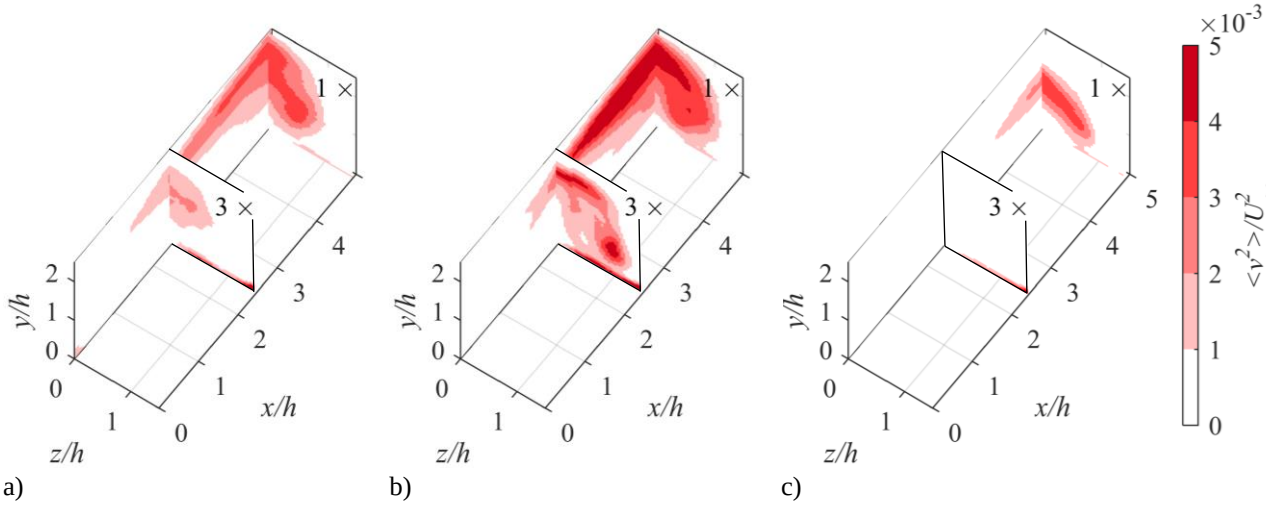

Fig. 12 Normalized wall-normal Reynolds stress $\langle v^2 \rangle / U_\infty^2$ for the a) wishbone, b) doublet, and c) ramp VGs.

To investigate the correlation of streamwise and wall-normal velocity fluctuation, the Reynolds shear stress $\langle uv \rangle$ normalized by U_∞^2 is shown in Fig. 13. The regions with negative $\langle uv \rangle / U_\infty^2$ have a major role in the production of turbulence. From the *x*-*y* planes, the largest negative $\langle uv \rangle / U_\infty^2$ is observed at the upper interface of the wake and the free-stream (i.e., a shear layer). The doublet VG presents the most intense negative Reynolds shear stress. The negative $\langle uv \rangle / U_\infty^2$ layer in the wake of the wishbone and doublet VGs begins more upstream than the ramp VG. To analyze the pattern from the *y*-*z* planes, a scaling factor of 3× is applied to the *y*-*z* planes at $x = 2.5h$ due to the relatively small magnitude of $\langle uv \rangle / U_\infty^2$ at this location. The negative $\langle uv \rangle / U_\infty^2$ is also extended in the spanwise direction in the wake of the wishbone and doublet VGs. Within the *y*-z planes at $x = 5h$, the negative $\langle uv \rangle / U_\infty^2$ region further expands and the magnitude gradually intensifies in all of the VG cases. The doublet VG generates the strongest negative $\langle uv \rangle / U_\infty^2$ while the ramp VG has the weakest negative $\langle uv \rangle / U_\infty^2$. Further, a positive $\langle uv \rangle / U_\infty^2$ region is present in the *x*-*y* planes below the core of the streamwise vortex. This is associated with the dominant motions from the first and third quadrant of velocity fluctuations (i.e., *v* versus *u*). Overall, the intensity of turbulent fluctuations is proportional to the VG wetted area.

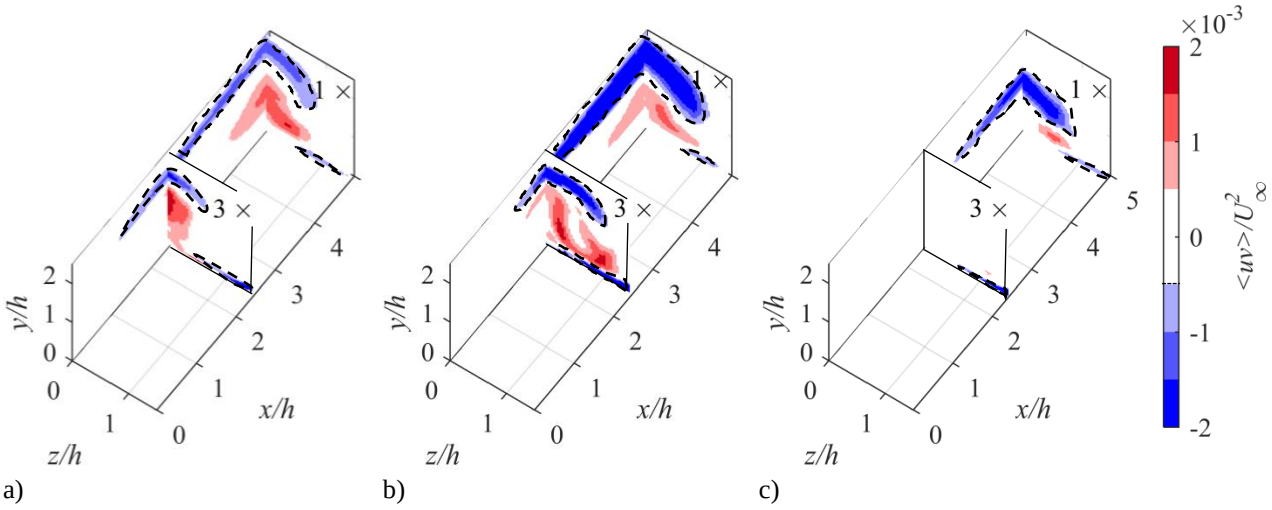

Fig. 13 Normalized Reynolds stress $\langle uv \rangle / U_\infty^2$ for the a) wishbone, b) doublet, and c) ramp VGs.

D. Turbulence production

The production of turbulent kinetic energy is investigated to determine the ability of the VGs to extract energy from the mean flow and generate small-scale turbulence. This process is expected to enhance small-scale mixing and contribute to the effectiveness of the VGs. The production of turbulence, P, is expressed with all terms as

$$P = -\left[\langle u^2 \rangle \frac{\mathrm{d}\langle U \rangle}{\mathrm{d}x} + \langle v^2 \rangle \frac{\mathrm{d}\langle V \rangle}{\mathrm{d}y} + \langle w^2 \rangle \frac{\mathrm{d}\langle W \rangle}{\mathrm{d}z} + \langle uv \rangle \frac{\mathrm{d}\langle U \rangle}{\mathrm{d}y} + \langle uv \rangle \frac{\mathrm{d}\langle V \rangle}{\mathrm{d}x} + \langle uw \rangle \frac{\mathrm{d}\langle U \rangle}{\mathrm{d}z} + \langle uw \rangle \frac{\mathrm{d}\langle W \rangle}{\mathrm{d}x} + \langle vw \rangle \frac{\mathrm{d}\langle V \rangle}{\mathrm{d}z} + \langle vw \rangle \frac{\mathrm{d}\langle W \rangle}{\mathrm{d}y}\right]. \quad (3)$$

The tomo-PIV data are used to calculate all of the production terms in Equation 3 due to the highly three-dimensionality of the turbulence in the wake of the VGs. A second-order central difference scheme is used to calculate the velocity gradients.

The turbulence production contours for the three VGs after being normalized by U_∞^2/h are shown in Fig. 14. Three different threshold levels are selected to demonstrate the variation of turbulence production within the measurement volume. The production contour in red (dark gray) has a threshold of 0.03, the orange (medium gray) contour has a threshold of 0.02, and the yellow (light gray) contour is constructed using a threshold of 0.006. As seen in Fig. 14a, the largest production behind the wishbone VG is concentrated along the centerline of the wake region within x = 0-1.8h, close to the shear layer between the upper interface of the wake and the free-stream. The intensity of production gradually decreases in both the spanwise and streamwise directions. The observation of Fig. 14b shows that the pattern of the doublet VG is similar to the wishbone VG, except the most intense production region persists farther until x = 3.5h. The contour from Fig. 14c illustrates that the ramp VG has a much weaker

turbulence production in terms of both iso-surface size and intensity compared to the other two VGs. The results show that the doublet VG extracts more turbulent kinetic energy from the mean flow. It also agrees with the large streamwise and wall-normal Reynolds stresses observed in the wake of doublet VG in Fig. 11 and Fig. 12.

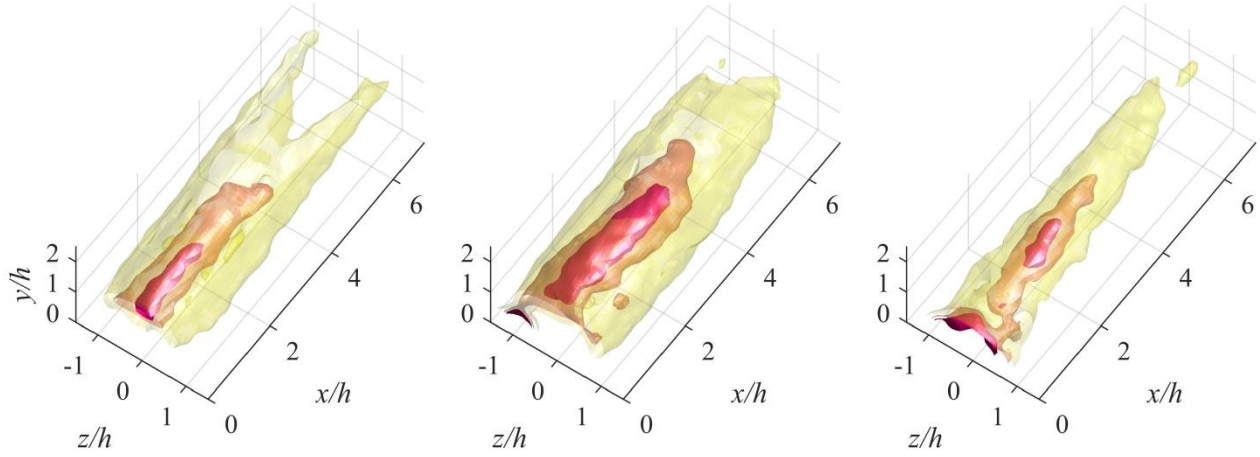

Fig. 14 Normalized turbulence production $P/(U_\infty^3 h)$ for the a) wishbone, b) doublet, and c) ramp VGs.

E. Vorticity field

The streamwise vortex in the VG wake is visualized using the normalized mean streamwise vorticity $\langle\Omega_x\rangle/(U_\infty^2/h^2)$ iso-surfaces as shown in Fig. 15. The positive streamwise vorticity is rendered in yellow (light gray) with a threshold of 0.015, and the negative streamwise vorticity is shown in red (dark gray) with a threshold of -0.015. A pair of counter-rotating vortex tubes is observed in the wake of all three VGs. With an increase in streamwise distance, the diameter of the vorticity tubes at the specified threshold gradually reduces for all VGs, which means that the vortices become weaker and diffused. In the wake of the wishbone VG, shown in Fig. 15a, the vortices are close to each other. The same pattern is also observed in the near-wake region of the doublet VG from Fig. 15b. However, as shown in the wake of the ramp VG from Fig. 15c, the spanwise gap between the vortices is much larger. It is believed that such a difference is created by the differences in VG geometry. The difference shows that the trailing edge of the wishbone VG and the second half-wedge of the doublet VG form the vortices close to the centerline. Overall, the wishbone VG produces the strongest steady vortex pair in the mean flow field, followed by the doublet and the ramp VGs.

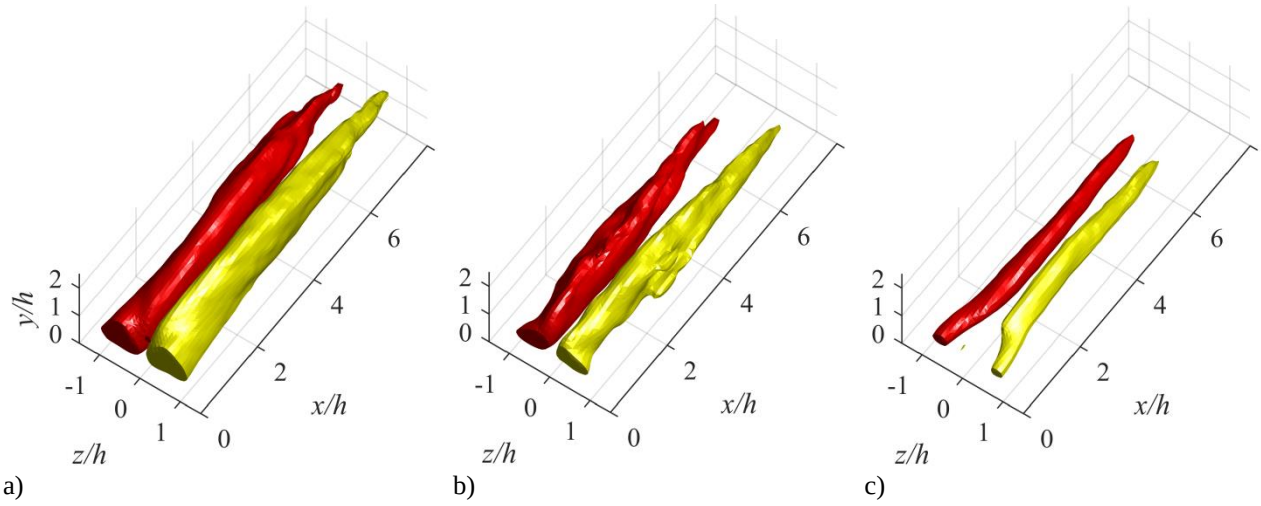

Fig. 15 Normalized mean streamwise vorticity $\langle\Omega_x\rangle/(U_\infty^2/h^2)$ iso-surfaces for the a) wishbone, b) doublet, and c) ramp VGs.

F. Three-dimensional flow visualization

Proper orthogonal decomposition (POD) of the three-dimensional fluctuating velocity fields from tomo-PIV has been carried out using the snapshot POD method [31, 32] to remove small-scale turbulence and noise. The energy distribution of the POD modes is also investigated to study the contribution of larger structures to the wake development. The percent of turbulent kinetic energy of each mode relative to the total turbulent kinetic energy for each VG is shown in Fig. 16a. The distribution of the energy of the modes for the doublet VG is very broad. However, for the wishbone and ramp VGs, the first two modes contain most of the energy. As seen in Fig. 16b, about 40% of the total energy is stored in the first 12 and 14 modes for the ramp and wishbone VGs, respectively. The doublet VG needs 18 modes to cover the same energy level. The difference in energy distributions reveals that the doublet VG produces more small-scale turbulence in its wake, which confirms the result that its wake has the highest level of turbulence.

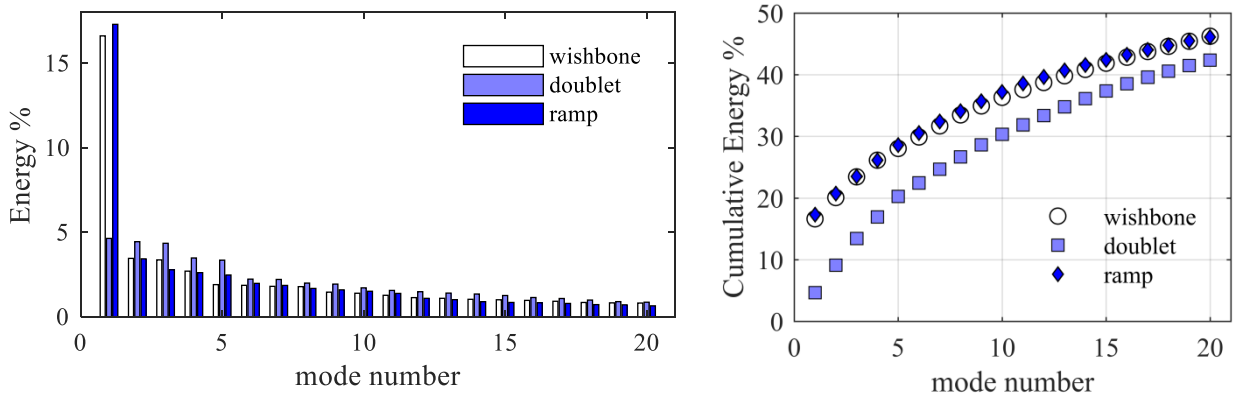

a) b)

Fig. 16 a) The distribution of turbulent kinetic energy of the POD modes, and b) cumulative energy distribution.

The spatial distribution of the vortex structures in the first POD mode is visualized in Fig. 17 for all three VGs. The vortex structures are identified using *Q*-criterion with a threshold of 0.3 s^{-2} for the wishbone and doublet VGs and 0.1 s^{-2} for the ramp VG. The thresholds are selected for clear visualization of the dominant structures without obstruction by the small-scale turbulence. As seen in Fig. 17a, the first POD mode of the wishbone VG has a pair of counter-rotating streamwise vortices. The vortex structures within the first mode of the doublet VG are chaotic such that the measurement volume is filled with small-scale vortices. This is consistent with the lower energy of this mode for the doublet in Fig. 17a. The ramp VG shows a weak trace of streamwise vortices. The high energy of the first mode indicates dominance of the steady streamwise vortices in the wake of the wishbone VG.

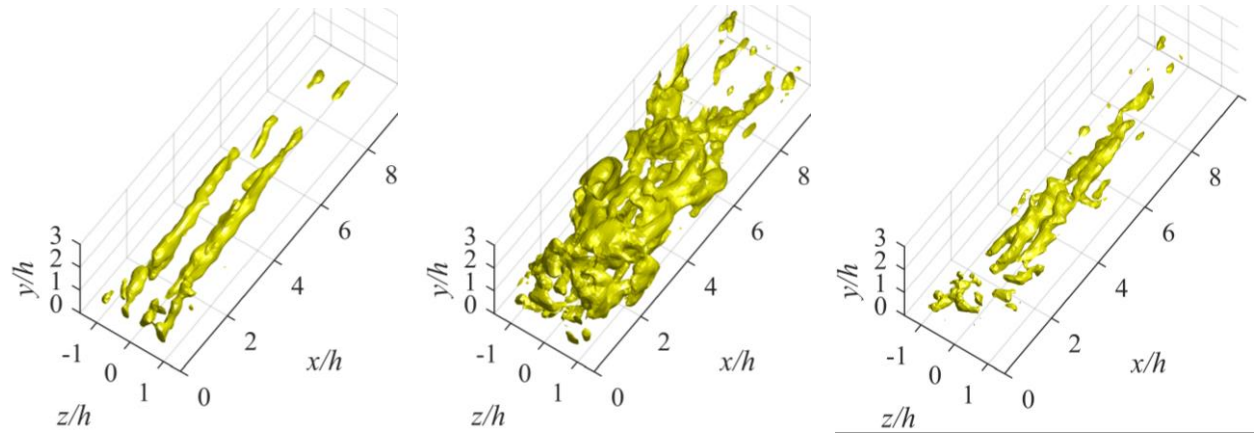

a) b) c)

Fig. 17 *Q*-criterion visualization of the dominant POD mode for the a) wishbone, b) doublet, and c) ramp VGs.

The dominant coherent structures of the instantaneous flow field are reconstructed using the mean flow with 40% of the turbulent kinetic energy and are shown in Fig. 18. The energy level is set to remove noise and small scale structures. Increasing the energy level does not change the shape of the dominant coherent structure. The visualization of the vortical structures is carried out using *Q*-criterion [33, 34] as shown within yellow ~~color~~ (light gray). The figures also show iso-surfaces of wall-normal fluctuating velocities in green (medium gray) and blue (dark gray), respectively. The fluctuating wall-normal velocity indicates the strength of the velocity (ejection or sweep) induced by the hairpin vortex. The shedding of hairpin-like vortex structures could readily be seen for all three VGs. In the wake of the wishbone VG, a pair of streamwise vortices is observed immediately after the trailing

edge of the VG. As seen in the animation, Supp_Video_S1.avi, the streamwise vortices are relatively steady and last until approximately $x = 5h$. The streamwise vortex pairs near the wall are believed to be the legs of the hairpin vortices. As expected, hairpin vortices appear to play a major role in the instantaneous flow field and development of the wake behind the wishbone VG. Due to the limited measurement volume in *y*-direction, the hairpin head is cropped as the structure moves downstream. In the animation, the transverse hairpin head is formed at the immediate downstream location of the VG trailing edge. It then connects to the streamwise vortices through the hairpin neck. As well, as seen in Fig. 18a, the hairpin vortex cannot be detected after $x = 6h$ due to the rapid reduction in vortex strength. In the wake of the doublet VG, a coherent streamwise vortex is not present, although Supp_Video_S2.avi shows occasional appearances of streamwise vortices between the hairpin legs. Higher levels of asymmetry and small-scale structures are observed in the wake of the doublet due to the interaction of the original vortex pair generated by the first half-body with the second half-body of the doublet VG. In Fig. 18b, the hairpin vortex is more irregular in shape compared with the other two cases. As a result, a broad distribution of mode energy was also observed in Fig. 16. Similar to the case of the wishbone VG, the head of the hairpin vortex in Fig. 18b is cropped in the *y*-direction downstream from the FOV. The evolution of the hairpin vortex from the wake of the ramp VG is presented in Fig. 18c and Supp_Video_S3.avi. The magnitude of the *Q*-criterion and wall-normal fluctuating velocity thresholds are 20 s^{-2} and 0.01 m/s, respectively, since the structures are weaker relative to those of the wishbone and doublet VGs. In the near-wake region, a pair of streamwise steady vortices could be observed between the hairpin legs and close to the wall. As shown in Fig. 18c, the hairpin vortices are coherent in strength and shape such that they can still be detected at the same *Q* threshold level even up to $x = 10h$. The height of the hairpin vortices from the wake of the ramp VG is about half the height of those from the wake of the wishbone and doublet VGs.

Overall, the hairpin vortices in the wake of the wishbone and doublet VGs are stronger, which indicates a more efficient wall-normal flow exchange of momentum when compared to the ramp VG. The generated vortex structures are about one third of the span of the VGs, which match the observation of the wake size from Fig. 5 and Fig. 6. The relatively steady streamwise vortices in the wake of the wishbone and ramp VGs are associated with their first POD modes with larger turbulent kinetic energy.

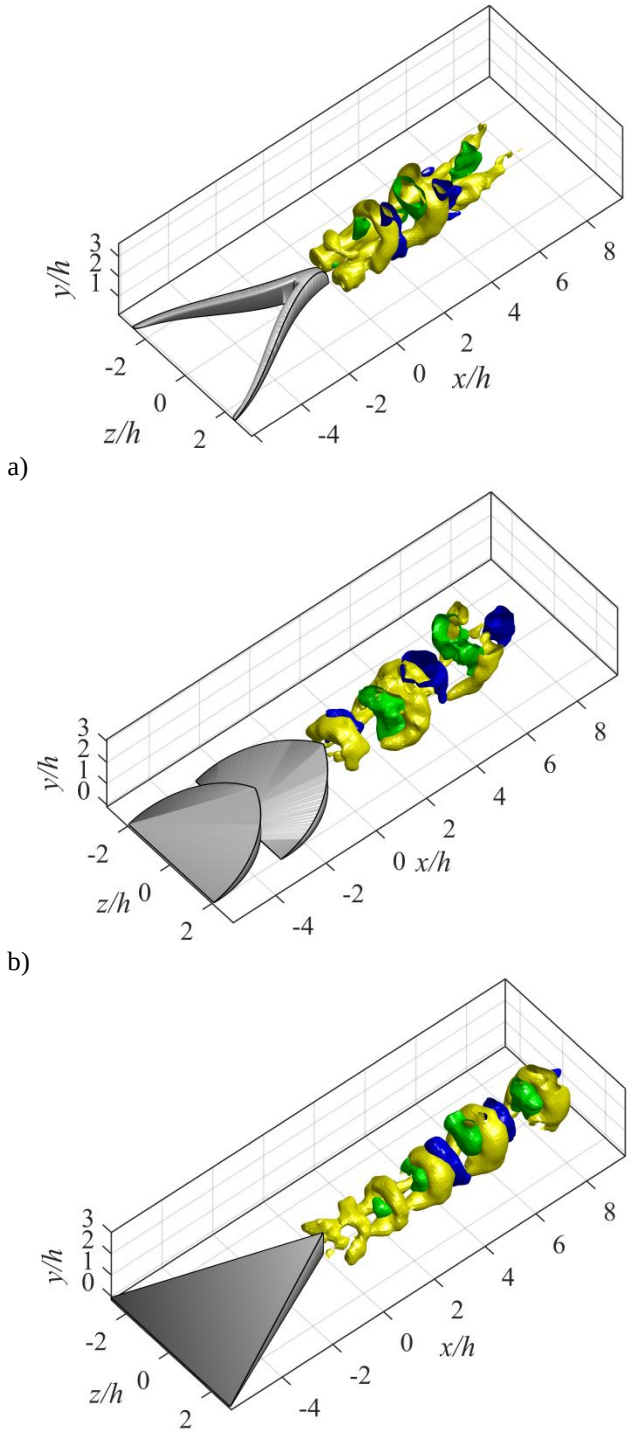

Fig. 18 Visualization of dominant coherent structure using *Q*-criterion and wall-normal fluctuating velocities for the a) wishbone, b) doublet, and c) ramp VGs.

The shedding frequency of the hairpin vortices for each VG was determined by applying a Discrete Fourier Transform (DFT) to the fluctuating wall-normal velocity along the centerline behind the trailing edge of the VGs.

The results of the DFT for each VG are given in linear spectral density (LSD) plots, which are shown in Fig. 19. The shedding frequencies of the VGs, given by the peaks of the LSD plots, are 10 Hz, 6 Hz, and 8 Hz for the wishbone, doublet, and ramp VGs, respectively. This suggests that the wishbone and ramp VGs may have more effective flow mixing than the doublet VG due to their higher shedding frequencies.

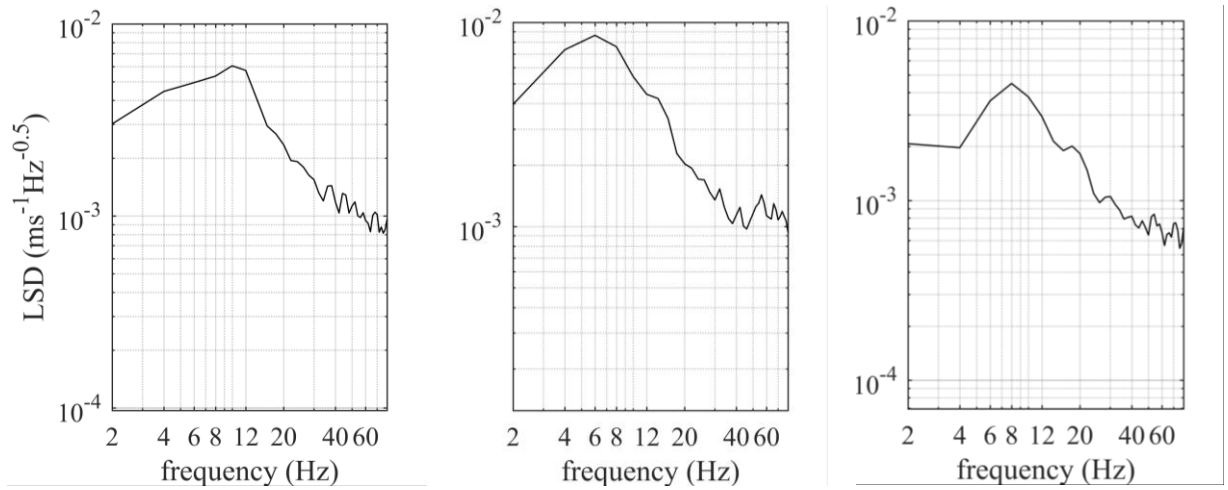

Fig. 19 LSD of *v* fluctuations for the a) wishbone, b) doublet, and c) ramp VGs.

G. VG performance

In this section, the performance of the VGs is evaluated using an estimation of drag and mixing performance in terms of VG ability to recover the wake deficit. The drag coefficient, C_D, of each VG is calculated here based on the momentum deficit of the wake. The conventional momentum deficit equation only considers the mean streamwise momentum flux as it applies to a steady flow or an instantaneous field. This may result in overestimation of the force for unsteady flows [35. 36]. Here we consider the method of Bohl and Koochesfahani [37], which includes the streamwise velocity fluctuation and downstream pressure deficit in the estimation of C_D through

$$C_D = -\frac{2}{c}\iint\left[\frac{\langle U\rangle}{U_\infty}\left(\frac{\langle U\rangle}{U_\infty}-1\right)+\varepsilon\left(\frac{\langle U\rangle}{U_\infty}-1\right)+\left(\frac{u_{rms}}{U_\infty}\right)^2-\left(\frac{v_{rms}}{U_\infty}\right)^2+\frac{1}{2}\left(1-\frac{U_0^2}{U_\infty^2}\right)\right]dydz\,, \quad (4)$$

where U_∞ and U_o are the free-stream velocity upstream and downstream of the VG (at the integration plane), respectively. The integration is carried out over a *y*-*z* control surface at $x = 5h$ using stereo-PIV data. The data covers -3*h* to 3*h*, and 0 to 6*h* in the *z* and *y* directions, respectively. In Equation 4, the term ε ($\langle U\rangle/U_\infty$-1) represents the variation of $\langle U\rangle$ along control surface, where ε is computed as 0.5-U_o/U_∞. The terms u_{rms} and v_{rms} are the velocity

fluctuations in the *x* and *y* directions, respectively. The effect of the pressure deficit is represented by the last two terms, derived from the *y*-component of the mean Navier-Stokes and Bernoulli equations [37].

The calculated C_D for the wishbone, doublet, and ramp VGs is 9.7×10^{-3}, 11.2×10^{-3}, and 6.4×10^{-3}, respectively. The result shows that the doublet VG produces the largest drag, followed by the wishbone and ramp VGs. The relation between C_D and the two wetted areas is plotted in Fig. 20a. No trend is observed between C_D and the two wetted areas in this figure. For example, C_D for the doublet VG is 15.4% more than the wishbone VG while the total wetted area is the same. The ramp VG has the smallest C_D while it has a larger VG wetted area than the wishbone. The relation between the energy of first POD mode and C_D of the VGs is also investigated in Fig. 21b. The energy of the first POD mode also shows no obvious correlation with the drag coefficient. Therefore, the geometric shape of the VG plays an important role on the wake organization and drag coefficient. It is not possible to predict the relative drag of VGs *a priori* based on a wetted area or the dominant vortical structures. However, the wishbone and doublet VGs have a larger drag than the ramp VG since they produced a spatially larger wake deficit and stronger vortices. Although the ramp VG has a larger wake deficit along the centerline, its wake is narrower and has the smallest C_D.

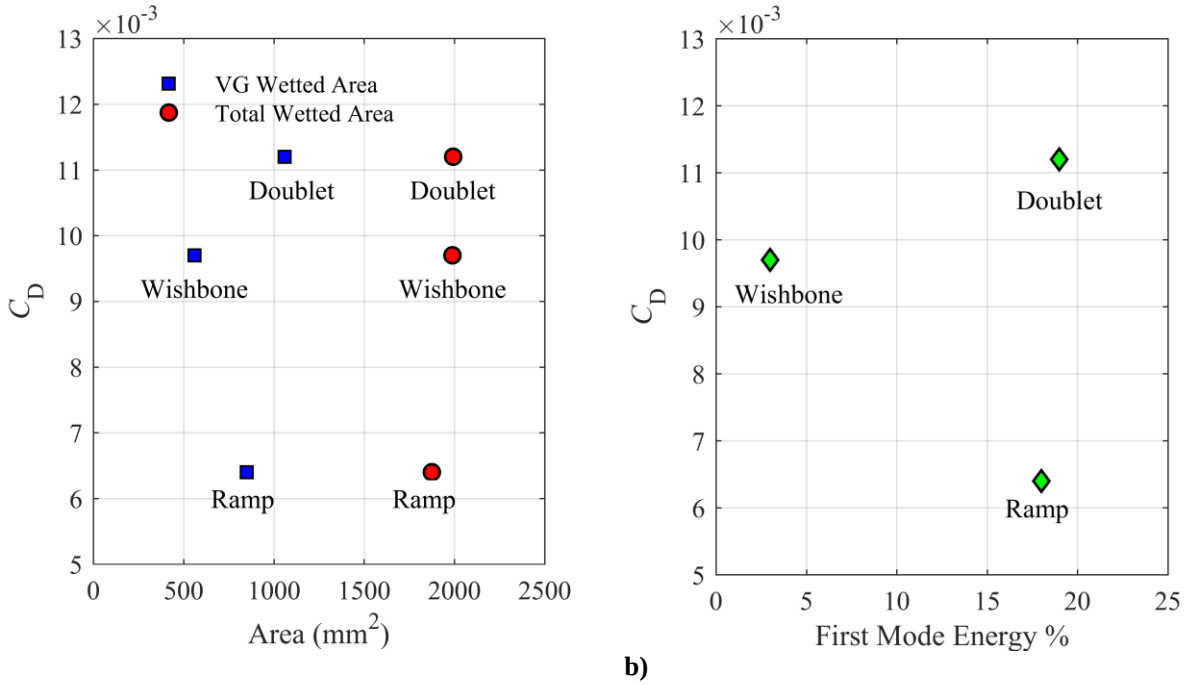

Fig. 20 Coefficient of drag versus a) wetted area and b) the first POD mode.

The strength of the VG in transporting the free-stream momentum towards the wall and filling up the wake deficit is evaluated here. The integral of $<U_{min}>/U_\infty$ along the wake centerline is used as an indication of velocity recovery; a

larger integral value means fast recovery due to an overall large value of $\langle U_{min} \rangle$. The integral of $\langle U_{min} \rangle / U_\infty$ is calculated from $x = 0$ to $5h$ using the planar-PIV data. The wake recovery number (e) is therefore defined as

$$e = \frac{1}{5h} \int_0^{5h} \frac{\langle U_{\min} \rangle}{U_\infty} \mathrm{d}x. \quad (5)$$

A large e indicates strong recovery of the wake (i.e. large $\langle U_{min} \rangle$). The integral is normalized by $5h$ to limit the maximum value of e to 1. The calculated wake recovery numbers are listed in Table 3. The results show that the wishbone VG has the strongest wake recovery number, followed by the doublet and ramp VGs. The wake recovery number of the wishbone VG is approximately 45% larger than the doublet VG, while the doublet and ramp VGs are only different by ~7%.

Table 3 also shows the e/C_D ratio to evaluate the overall performance of the VGs. A larger e/C_D is favorable since it represents a strong wake recovery with low device drag. The result of the ratio e/C_D reveals that the wishbone VG has the best performance in terms of improving flow mixing with low parasitic drag. The ramp VG presents a similar e/C_D relative to the wishbone VG since it has a small device drag. The doublet VG shows the worst performance due to its large device drag.

Table 3 Evaluation of wake recovery and drag of the VGs.

VG	e	C_D	e/C_D
Wishbone	0.45	0.0097	47
Doublet	0.31	0.0112	28
Ramp	0.29	0.0064	46

V.Conclusion

Three non-conventional VGs of different shapes but similar dimensions are investigated by evaluating the wake flow using planar-, stereo-, and high-speed tomo-PIV measurements. The VGs are 3D printed and placed in the laminar boundary layer of a flat plate submerged in a water channel. Turbulence statistics and the evolution of vortical structures were investigated in the wake of the VGs. The performances of the VGs were compared in terms of wake deficit recovery and parasitic drag.

The investigation of the mean velocity field demonstrated that the doublet VG has the largest wake region, which suggests a larger pressure drag. There was a small backward flow region and a large velocity deficit in the near-wake region of the doublet and ramp VGs, associated with their larger VG wetted area. There were also two local minima in the wake of the doublet VG due to the flow interaction with the two successive half-bodies of this geometry. On the other hand, the velocity deficit in the wake of the wishbone VG recovered faster than the other two VGs.

The largest wall-normal and spanwise mean velocity is observed in the wake of wishbone VG, suggesting more mixing between the free-stream and the low-speed near-wall flow. The doublet VG was shown to have the second largest wall-normal transport of flow while the ramp VG presented the smallest wall-normal motion. This has also been confirmed from the analysis of mean vorticity, such that the wishbone VG produces the strongest counter-rotating streamwise vortices. Conversely, the ramp VG has the weakest streamwise vortices with the smallest spanwise distance (i.e., a narrower wake). The experimental results also demonstrated that the counter-rotating streamwise vortices are the dominant vortical pattern of the mean flow field for all three VGs. The pairs induce an upward flow motion at the centerline of the wake surrounded on both sides by regions of downward flow.

A narrow layer with high turbulence intensity is formed at the interface of the wake and free-stream for all VGs. This layer thickens with an increase of streamwise distance and has the largest intensity in the wake of the doublet VG. The doublet VG has the largest streamwise, wall-normal, and shear Reynolds stress, followed by the wishbone and ramp VGs. The estimation of the turbulence production using the tomo-PIV data also indicates that the doublet VG generates the largest turbulence kinetic energy. This suggests that the generated turbulence is approximately proportional to the VG wetted area.

The dominant coherent structure is determined to be a hairpin vortex instead of steady streamwise counter-rotating vortices in the instantaneous flow field. The POD analysis showed that the distribution of turbulent kinetic energy of the modes for the doublet VG is broader than the wishbone and ramp VGs. Therefore, the doublet VG produces more small-scale turbulence structures compared to the other two VGs. The first POD mode for the wishbone and ramp VGs contains a large amount of turbulent kinetic energy and is explained by the existence of a pair of relatively steady streamwise vortices. Visualization using Q-criterion also revealed that the hairpin vortices generated by the ramp VG are coherent in terms of both strength and shape. However, the hairpin vortices of the ramp are weaker than the ones generated by the other two VGs.

The overall performance of the VGs was compared using an estimation of drag and wake recovery. The VG drag was estimated based on momentum deficit and showed that the doublet and ramp VGs have the largest and the smallest drag coefficients, respectively. The wishbone VG has the best performance in terms of the recovery of the wake deficit, followed by the ramp and doublet VGs. When the overall performance is evaluated in terms of the ratio of wake recovery number to drag coefficient, the wishbone and ramp VGs have a similar performance while

the doublet has the weakest performance. The high performance of the wishbone is due to its high mixing strength while the high performance of the ramp VG is mostly associated its lower drag.

VI.References

[1] Simpson, R. L., "Review-a review of some phenomena in turbulent flow separation." *ASME Journal of Fluids Engineering*, Vol.103, No.4, 1981, pp. 520-533.
doi: 10.1115/1.3241761

[2] Ashjaee, J., and Johnston, J. P., "Straight-Walled, Two-Dimensional Diffusers—Transitory Stall and Peak Pressure Recovery," *Journal of Fluids Engineering*, Vol. 102, 1980, p. 275.
doi: 10.1115/1.3240680

[3] Schubauer, G. B., and Spangenberg, W. G., "Forced mixing in boundary layers." *Journal of Fluid Mechanics*, Vol.*8, No.*1, 1960, pp. 10-32.
doi: 10.1017/S0022112060000372

[4] Taylor, H. D., "The elimination of diffuser separation by vortex generators." United Aircraft Corporation, East Hartford, CT, Technical Report No R-4012-3, June 1947.

[5] Kuethe, A. M., "Effect of streamwise vortices on wake properties associated with sound generation." *Journal of Aircraft*, Vol.9, No.10, 1972, pp.715-719.
doi: 10.2514/3.44333

[6] Lin, J. C., "Control of turbulent boundary-layer separation using micro-vortex generators." *30th Fluid Dynamics Conference*. 1999.
doi: 10.2514/6.1999-3404

[7] Wheeler, G. O., "Means of Maintaining Attached Flow of a Flow Medium," U.S. Patent No. 4455045, 1991.

[8] Wheeler, G. O., "Low Drag Vortex Generators," U.S. Patent No. 5058837, 1991.

[9] Lin, J. C., "Control of a Low-speed Turbulent Flow Over a Backward-facing Ramp." PhD Dissertation, Old Dominion University, 1990.

[10] Godard, G., and Michel S., "Control of a decelerating boundary layer. Part 1: Optimization of passive vortex generators." *Aerospace Science and Technology*, Vol.10, No.3, 2006, pp. 181-191.
doi: 10.1016/j.ast.2005.11.007

[11] Forster, K. J., and White, T. R., "Numerical investigation into vortex generators on heavily cambered wings." *AIAA Journal*, Vol.52, No.5, 2014, pp. 1059-1071.
doi: 10.2514/1.J052529

[12] Lin, J. C., Howard, F. G., and Selby, G. V., "Investigation of several passive and active methods for turbulent flow separation control."*21st Fluid Dynamics, Plasma Dynamics and Lasers Conference*. 1990.
doi: 10.2514/6.1990-1598

[13] Lin, J. C., Howard, F. G., and Selby, G. V., "Exploratory study of vortex-generating devices for turbulent flow separation control." *29th Aerospace Sciences Meeting, Aerospace Sciences Meetings*, January 1991.
doi: 10.2514/6.1991-42

[14] Lin, J. C., Howard, F. G., and Selby, G. V., "Small submerged vortex generators for turbulent flow separation control." *Journal of Spacecraft and Rockets*, Vol. 27, No.5, 1990, pp. 503-507.
doi: 10.2514/3.26172

[15] Lin, J. C., "Review of research on low-profile vortex generators to control boundary-layer separation." *Progress in Aerospace Sciences*, Vol.38, No.4, 2002, pp. 389-420.
doi: 10.1016/S0376-0421(02)00010-6

[16] Betterton, J., Hackett, K., Ashill, P., Wilson, M., and Woodcock, I., "Laser doppler anemometry investigation on sub boundary layer vortex generators for flow control." *10th International Symposium on Applications of Laser Techniques to Fluid Mechanics*, 2000, pp. 10–13.

[17] Janiszewska, J., Gregorek, G., and Lee, J., "The LS(1)-0417MOD Airfoil Aerodynamic Flow Characteristcs with the Application of Vortex Generators," *42nd AIAA Aerospace Sciences Meeting and Exhibit*, Reston, Virigina: American Institute of Aeronautics and Astronautics, 2004, pp. 1–10.
doi: 10.2514/6.2004-661

[18] Rao, D., and Kariya, T., "Boundary-layer submerged vortex generators for separation control - An exploratory study," *1st National Fluid Dynamics Conference*, Reston, Virigina: American Institute of Aeronautics and Astronautics, 1988.
doi: 10.2514/6.1988-3546

[19] Barrett, R., and Farokhi, S., "On the aerodynamics and performance of active vortex generators," *11th Applied Aerodynamics Conference*, Reston, 1993, pp. 376–386.
doi: 10.2514/6.1993-3447

[20] Wendt, B. J., and Hingst, W. R., "Flow structure in the wake of a wishbone vortex generator." *AIAA Journal*, Vol.32, No.11, 1994, pp. 2234-2240.
doi: 10.2514/3.12282

[21] Acarlar, M. S., and Smith, C. R., "A study of hairpin vortices in a laminar boundary layer. Part 1. Hairpin vortices generated by a hemisphere protuberance." *Journal of Fluid Mechanics*, Vol. 175, 1987, pp. 1-41.
doi: 10.1017/S0022112087000272

[22] Sun, Z., Schrijer, F. F. J., Scarano, F., and van Oudheusden, B. W., "Decay of the supersonic turbulent wakes from micro-ramps." *Physics of Fluids*, Vol.26, No.2, 2014, pp. 025115.
doi: 10.1063/1.4866012

[23] Ye, Q., Schrijer, F. F., and Scarano, F., "Boundary layer transition mechanisms behind a micro-ramp." *Journal of Fluid Mechanics*, Vol.793, 2016, pp. 132-161.
doi:10.1017/jfm.2016.120

[24] Sun, Z., "Micro Vortex Generators for Boundary Layer Control: Principles and Applications." *International Journal of Flow Control*, Vol. 7.1-2, 2015.
doi: 10.1260/1756-8250.7.1-2.67

[25] Schlichting, H., and Klaus G., "Fundamentals of Boundary-Layer Theory." *Boundary-Layer Theory*, 9th ed., Springer, Berlin Heidelberg, 2016, pp. 31.
doi: 10.1007/978-3-662-52919-5

[26] Westerweel, J., Scarano, F., "Universal outlier detection for PIV data." *Experiments in Fluids*, Vol.39, No.6, 2005, pp. 1096-1100.
doi: 10.1007/s00348-005-0016-6

[27] Wieneke, B. "Volume self-calibration for 3D particle image velocimetry." *Experiments in Fluids*, Vol.45, No.4, 2008, pp. 549-556.
doi: 10.1007/s00348-008-0521-5

[28] Elsinga, G. E., Scarano, F., Wieneke, B., and van Oudheusden, B. W., "Tomographic particle image velocimetry." *Experiments in Fluids*, Vol.41, No.6, 2006, pp. 933-947.
doi: 10.1007/s00348-006-0212-z

[29] Scarano, F., and Poelma, C., "Three-dimensional vorticity patterns of cylinder wakes." *Experiments in Fluids*, Vol.47, No.1, 2009, pp. 69.
doi: 10.1007/s00348-009-0629-2

[30] Pope, S. B., "Turbulent flows." *Cambridge University Press*; 2000.
doi: 10.1007/s00348-009-0629-2

[31] Lumley, J. L., "The structure of inhomogeneous turbulent flows." *Atmospheric Turbulence and Radio Avie Propagation*, 1967, pp. 166-178.

[32] Sirovich, L., "Turbulence and the dynamics of coherent structures. I. Coherent structures." *Quarterly of Applied Mathematics*, Vol. 45, No.3, 1987, pp. 561-571.
doi: 10.1090/qam/910463

[33] Kolář, V., "Vortex identification: New requirements and limitations." *International journal of heat and fluid flow* , Vol. 28, No.4, 2007, pp. 638-652.
doi: 10.1016/j.ijheatfluidflow.2007.03.004

[34] Hunt, J. C., Wray, A. A. and Moin, P. "Eddies, streams, and convergence zones in turbulent flows." *Studying Turbulence Using Numerical Simulation Databases*, *Proceedings of the 1988 Summer Program*, 1988, pp. 193-208.

[35] Ramamurti, R., and Sandberg, W., "Simulation of flow about flapping airfoils using finite element incompressible flow solver." *AIAA*, Vol.39, No.2, 2001, pp. 253-260.
doi: 10.2514/2.1320

[36] Koochesfahani, M. M., "Vortical patterns in the wake of an oscillating airfoil." *AIAA*, Vol.27, No.9, 1989, pp. 1200-1205.
doi: 10.2514/3.10246

[37] Bohl, D. G., and Koochesfahani, M. M. “MTV measurements of the vortical field in the wake of an airfoil oscillating at high reduced frequency.” *Journal of Fluid Mechanics*, Vol. 620, 2009, pp. 63-88. doi: 10.1017/S0022112008004734